Section 5

Development of and studies with regional and smaller-scale atmospheric models, regional ensemble, monthly and seasonal forecasting

The 2010 upgrades of the Météo-France NWP system

Ludovic Auger, Eric Bazile, Loïk Berre, Pierre Brousseau, Yves Bouteloup, François Bouttier, François Bouyssel, Laurent Descamps, Gérald Desroziers, Nadia Fourrié, Elizabeth Gérard, Vincent Guidard, Alain Joly, Fatima Karbou, Carole Labadie, Cécile Loo, Valéry Masson, Patrick Moll, Christophe Payan, Jean-Marcel Piriou, Florence Rabier, Laure Raynaud, Olivier Rivière, Yann Seity, Eric Sevault, Françoise Taillefer, Eric Wattrelot, Karim Yessad

CNRM/GAME, Météo-France and CNRS
francois.bouttier@meteo.fr

1. Progress report

A major upgrade of the global and regional prediction systems at Météo-France was implemented on 6 April 2010. The AROME-2.5km regional prediction system over mainland France has been modified as follows:

- increase of the number of vertical levels from 41 to 60 levels, the corresponding enhancement of vertical resolution is mainly located in the lower troposphere

- activation of an absorbing upper boundary condition with relaxation of the large-scales to the NWP boundary condition model

- change of the boundary condition model from the regional ALADIN-France to the global ARPEGE system, with hourly updated lateral and upper boundary conditions

- update of the background error covariance model used by the AROME 3DVar data assimilation

- use of flow-dependent background error variances provided by the ARPEGE ensemble assimilation system

- assimilation of AIRS, IASI and SSM/I radiances; implementation of a variational bias correction scheme for the assimilation of SEVIRI radiances; radiances are used with an increased density

- assimilation of radar reflectivities through Bayesian retrievals of vertical humidity profiles *(described elsewhere in this volume)*

- upgrades to the EDKF shallow convection scheme

- implementation of fog sedimentation

- improvement of the gust diagnostic computation.

The ARPEGE global prediction system has been modified as follows:

- increase of the model horizontal resolution from T538 to T798 stretched spectral truncation i.e. from 15 to 10.5km resolution over Western Europe (and to 60km over the South Pacific)

- increase of the model vertical resolution from 60 to 70 levels, most of the enhancmeent is located in the lower troposphere

- increase of the 4DVar assimilation increment resolution from T224 to T323 i.e. from 90 to 60km

- increase of the density of assimilated satellite radiances to 125km

- activation of extra radiance data in the 4DVar data assimilation: AMSU-B channel 5 over land *(see contribution by F. Karbou et al elsewhere in this volume)*, IASI water vapour channels, and the NOAA19 satellite.

- assimilation of MODIS clear-sky water vapour winds

- increased dependency of the ARPEGE 4DVar assimilation on the ensemble assimilation system, which provides flow-dependent background error variances for all mass and wind control variables.

- improvement of the turbulent kinetic energy scheme and of the 4DVar simplified physics

- improvement of the gust diagnostic computation

The ALADIN regional systems has inherited from the ARPEGE modifications, the ALADIN horizontal resolution is now 7.5km over France and 8km over the SW Indian Ocean.

The ARPEGE ensemble prediction system (PEARP) has been upgraded in December 2009:

- increase of the number of members from 11 to 35

- increase of the vertical resolution from 55 to 65 levels

- initial perturbations are derived from the ARPEGE ensemble assimilation, on top of the previously used singular vectors.

- model error is represented in the forecasts using varying physical parametrization setups.

- more frequent ensemble forecasts (from the 06 and 18UTC analyses; previously, PEARP was only run from the 18UTC analysis)

The ARPEGE ensemble assimilation system, which now runs 6 members at T399 uniform resolution (i.e. 50km) has been upgraded to use 4DVar (3DVar was previously used) with 190-km increments. *(described elsewhere in this volume)*

The combined impact of the above changes is beneficial in terms of most forecast scores at large and regional scale. They have received favourable subjective evaluations both in routine forecasts and in severe weather events such as the Xynthia storm that hit Southwestern Europe on 27/28 February 2010. The corresponding software developments have been included into the IFS/ARPEGE software that is used by ECMWF and the ALADIN and HIRLAM consortia.

2. Plans for 2010

Operational upgrades of the above systems in 2010 will at least include:

- a substantial increase in geographical extent of the AROME-France model, which will encompass the cities of Madrid, Rome, Prague, Hamburg, Shannon.

- the implementation of a high-resolution surface data assimilation for AROME.

- an upgrade of the PEARP global ensemble prediction system, which will reach 15km resolution over Western Europe.

- enhancements to the use of satellite radiances, including cloud-affected IR radiances, higher-resolution IASI radiances

Various model components will be upgraded for future operational applications, including improvements to the ARPEGE convection scheme and the representation of convection and fog in AROME. New configurations are being developed, including an enhanced ALADIN system for operational high-resolution NWP over tropical regions (West Indies, Guyana, Polynesia, Southwestern Pacific), a convective-scale ensemble prediction system, a 500m-resolution version of AROME, and a rapid refresh version of AROME for nowcasting and air traffic management applications.

Fog Prediction from a Multimodel Mesoscale Ensemble Prediction System

Jun Du (Jun.Du@noaa.gov), Binbin Zhou, and Geoff DiMego
National Centers for Environmental Prediction (NCEP)/NOAA, Washington, D.C

A new diagnostic fog-detection scheme

Liquid Water Content (LWC) at the model's lowest level was commonly used to represent fog in previous studies. However, the LWC-only approach doesn't work well in an operational NWP model for the following two reasons: too coarse spatial resolution to properly resolve important physics in fog near the surface, and physics schemes or parameterizations not tailored for near-ground fog but for precipitation or clouds at higher levels. As a result, the LWC from NWP models is usually not reliable enough to represent fog and tends to seriously under-forecast fog in many cases. To better detect fog, other variables besides LWC should be considered. Considering that fog has different types with different formation mechanisms, e.g., some build from stratus-subsidence, some from advection, and some from radiation cooling near the ground, a new multi-variable based diagnostic fog-detection scheme is proposed as follows:

LWC at model lowest level ≥ 0.015 g/kg, OR
Cloud Top ≤ 400 m AND Cloud Base ≤ 50 m, OR
10-Wind Speed ≤ 2 m AND 2m-RH ≥ 90 %

Results

Using a 10-member 15km multimodel mesoscale ensemble prediction system (Zhou and Du, 2010), various verifications of fog forecasts were performed including deterministic (left figure), probabilistic (right figure) scoring measures as well as individual cases (not shown) over Eastern China from February to August 2008. Left Figure shows how the deterministic fog forecast skill improves with various approaches, while Right Figure shows how multimodel ensemble outperforms single-model ensembles in probabilistic forecasts.

Summary of the study

A new multivariable based diagnostic fog-forecasting method has been developed at NCEP. Since all the five base variables used for the diagnosis are direct outputs from a model, this fog diagnostic algorithm can be included as part of the model post-processor and, therefore, the fog forecast can now be provided conveniently and centrally as a direct NWP model guidance.

Applying the various approaches including the new fog detection scheme, ensemble technique, multi-model approach and the increase in ensemble size, the improvement in fog forecast accuracy was steady in each of the approaches and dramatic: from a basically no-skill-at-all (Equitable Threat Score=0.063) to a skill level equivalent to that of warm-season precipitation forecasts of the current state-of-the-art NWP models (0.334). In specific, (1) The multivariable based fog diagnostic method has a much higher detection capability than LWC-only based approach (a commonly used method in current practice). The latter has a very low detection rate and tends to miss almost 90% of fog events; the former can greatly improve the fog detection rate; (2) The ensemble-based forecasts are, in general, superior to a single forecast measured both deterministically and probabilistically. The case study also demonstrates that ensemble approach could provide more societal value than a single forecast to end-users especially for low-probability significant events like fog. Deterministically, a forecast close to the ensemble median (50% probability) is particularly helpful; (3) The reliability of probabilistic forecasts can be effectively improved by using a multi-model ensemble instead of a single-model ensemble. For small-size ensemble such as the one in this study, the increase in ensemble size is also important in improving probabilistic forecasts although such an importance is expected to decrease with the increase in ensemble size (Du et. al, 1997). For the detail of this study, readers are referred to Zhou and Du (2010).
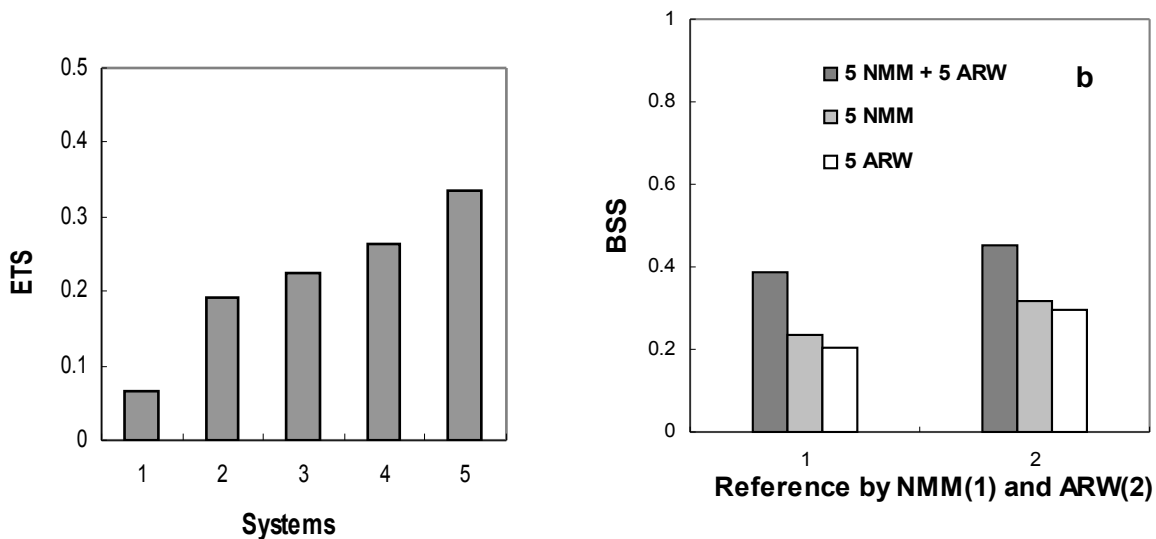
Left Figure. Equitable Threat Scores (ETSes, averaged of the two models, NMM and ARW, over the 7-month period at 12- and 36-h forecast lengths) from the various forecast systems: 1) the single control runs based on the LWC-only approach (ETS=0.063), 2) the single control runs but based on the new multivariable fog diagnosis (0.192; a 205% improvement over the previous step), 3) the 40% probability forecasts based on the 5-member single model ensembles (0.225; 17.2%),

Statistical verification of short range forecasts by NHM and WRF-ARW over Southeast Asia and Japan areas

Syugo HAYASHI

Meteorological Research Institute / Japan Meteorological Agency

Email: shayashi@mri-jma.go.jp

Statistical verifications of the numerical weather prediction by JMA's non-hydrostatic model (NHM; Saito et al., 2006) are needed for the prevention and mitigation of meteorological disasters in Southeast Asia, because NHM have seldom been executed in tropical region. For the validation of the verifications of NHM, WRF-ARW (Skamarock et al. 2005) was also conducted with the same conditions of NHM. The verification results of the both models were compared for the confirmation of the statistical accuracy of their forecasts.

In the both models, same domain size, same time step and same initial / boundary data were used for fair comparison. Initial / boundary condition were given by NCEP-GFS forecast in every 3-hour. Experiential settings were not changed from the model's own recommended namelists. The domains of the models are shown in Fig. 1. They had 160 x 160 x 40 grids with 20 km in horizontal and 301 x 301 x 40 grids with 5 km resolution. The top heights of the models were 22km (about 45hPa). Two Simulation periods were selected. One is "July 2007 (31 days)" for Japan region, the other is "January 2008 (31 days)" for Southeast Asia region.

Figures 2a-d plot the bias and threat scores against the precipitation intensity (mm / 3 hours) by satellite observation (CMORPH). In Japan region, the bias score (fig. 2a) is close to 1 in weak precipitation intensity. The bias score in heavy precipitation is overestimated, because CMORPH doesn't have good score in heavy rain case. Using surface rain observation, the bias
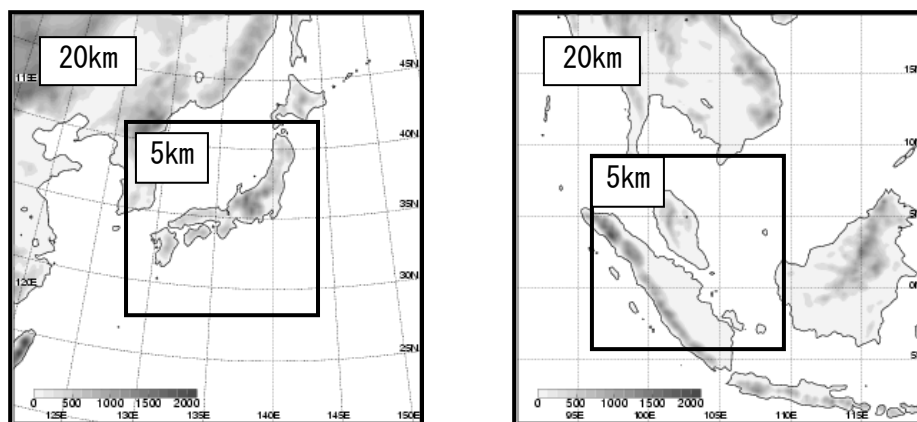
Fig. 1 Model domain and topography for Japan region and Southeast Asian region, with 20km horizontal resolution and 160 x 160 grid (3200 km square), with 5km horizontal resolution and 301 x 301 grid (1500 km square).
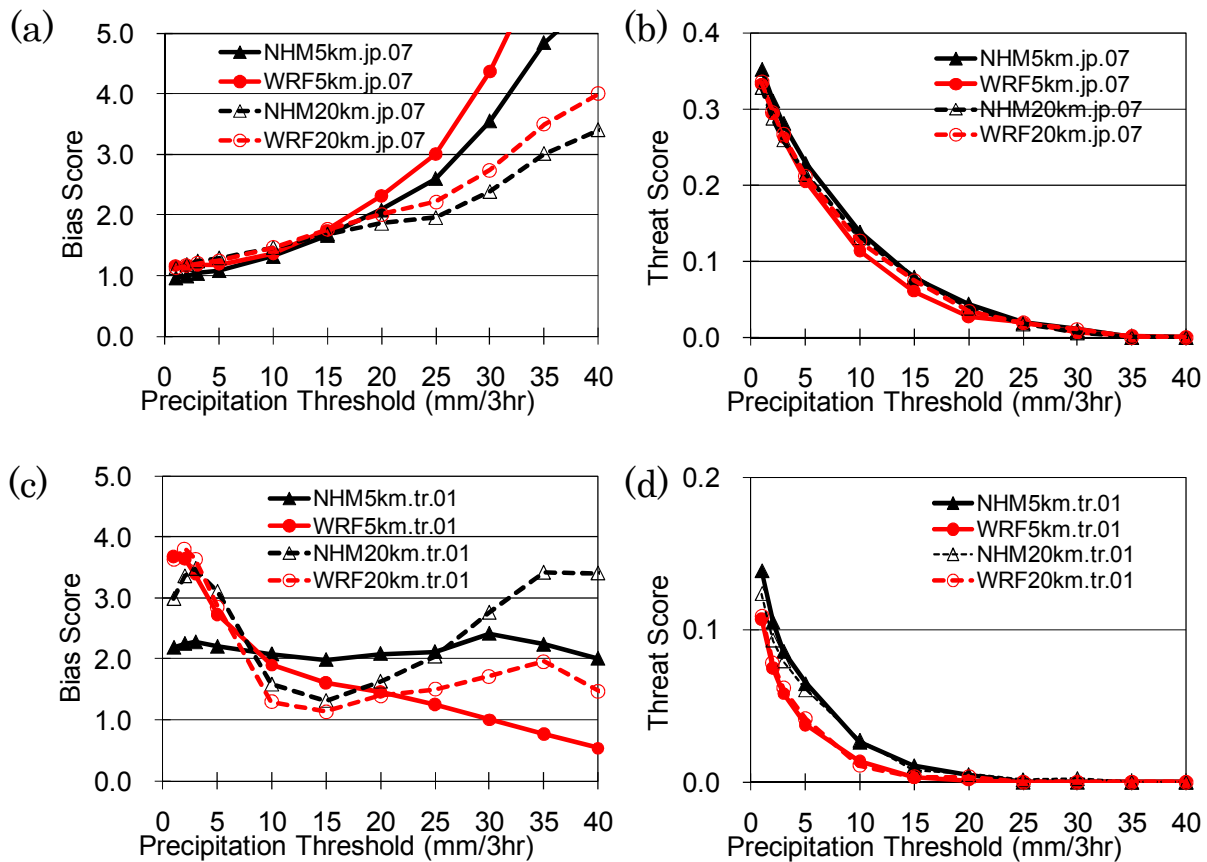
Fig. 2 Bias score and threat score of 3hr-precipitation against CMORPH (satellite).
(a) Bias score, and (b) threat score Japan region.
(c) Bias score, and (d) threat score Southeast Asian region.
Triangles are NHM, circles are WRF, Solid lines are 5km, dashed lines are 20km.

score in heavy rain is close to 1 (not shown). The threat score (fig. 2b) is 0.35 at 1 mm / 3 hours in the both models. This is reasonable accuracy because it is similar to JMA's operational score (0.3~0.4) in this region. The bias score in Southeast Asian region is shown in Fig. 3c. All models exceed the 1 in the bias score. The threat scores of Southeast Asian region (Fig. 4d) is a half of the scores in that of Japan region. We are investigating the cause of this deterioration. So, more improvements should be done for the simulations in low-latitude.

References

Saito K., T. Fujita, Y. Yamada, J. Ishida, Y. Kumagai, K. Aranami, S. Ohmori, R. Nagasawa, S. Kumagai, C. Muroi, T. Kato, H. Eito and Y. Yamazaki, 2006: The Operational JMA Nonhydrostatic Mesoscale Model. Mon. Wea. Rev. 134, 1266–1298.

Skamarock, W.C., J.B. Klemp, J. Dudhia, D.O. Gill, D.M. Barker, W. Wang, and J.G. Powers, 2005: A Description of the Advanced Research WRF Version 2. NCAR Tech. Note, 468, 88p.

Fuzzy Verification of Hydrometeors in a High-resolution Model Using a Radar Simulator

Yasutaka Ikuta[1] and Yuki Honda[2]

Numerical Prediction Division, Japan Meteorological Agency

The Japan Meteorological Agency (JMA) has been developing a local analysis-forecast system called the Local Forecast Model (LFM) with a horizontal resolution of 2 km to enhance information for disaster prevention and aviation forecasts. The LFM is composed of the NHM (Saito et al., 2006) as a forecast model and a rapid update cycle based on the 3D-Var version of JNoVA (Honda et al., 2005) as the local analysis system. One of its most important products is a very-short range quantitative precipitation forecast (VSRF). The LFM employs only a cloud microphysics scheme without convective parameterization in the moist process. Accordingly, accuracy improvement for forecast hydrometeors in cloud microphysics is expected to improve VSRF. However, no regularly observed hydrometeor data are available as reference values to verify the three-dimensional distribution of forecast hydrometeors. Therefore, simulated radar reflectivity using model-predicted hydrometeors are evaluated against observed radar reflectivity data. To simulate radar reflectivity, we developed a radar simulator following Caumont and Coauthors (2006). In addition, the fractions skill score (FSS) (Roberts and Lean, 2008) is adopted as a statistical metric to mitigate the well-known problems in high-resolution verification caused by displacement error.

As cloud microphysics for the NHM in the LFM, one-moment and two-moment schemes of bulk microphysical parameterization (BMP) are currently being tested. The experiments using one-moment and two-moment BMP are referred to as BMP-1 and BMP-2, respectively. Figure 1 shows the FSSs of the simulated reflectivity for BMP-1 and BMP-2. The FSSs of BMP-2 are larger than those of BMP-1 within a 30-dBZ threshold (Figure 1 (a)), and the middle-elevation ($1.4° - 3.0°$) scores are better than other elevation scores in a spatial scale larger than 40 km. However, the percentile FSSs at a high elevation are larger than those at a low elevation (Figure 1 (b)) because the detectable range permitting verification of the reflectivity peak represented by the percentile is limited at high elevations. Figure 2 shows that the FSS target skill could detect BMP-2 as a good forecast with a large threshold and a wide spatial scale, but the BMP-2 score at low elevation ($0.0°$) became slightly worse than that of BMP-1.

Verification using the FSS applied to simulated radar reflectivity reveals the characteristics of the elevation dependency of one-moment and two-moment BMP. This verification method is therefore considered to represent a skillful approach for hydrometeor verification.

---

[1] ikuta@met.kishou.go.jp
[2] honda.yuuki@met.kishou.go.jp
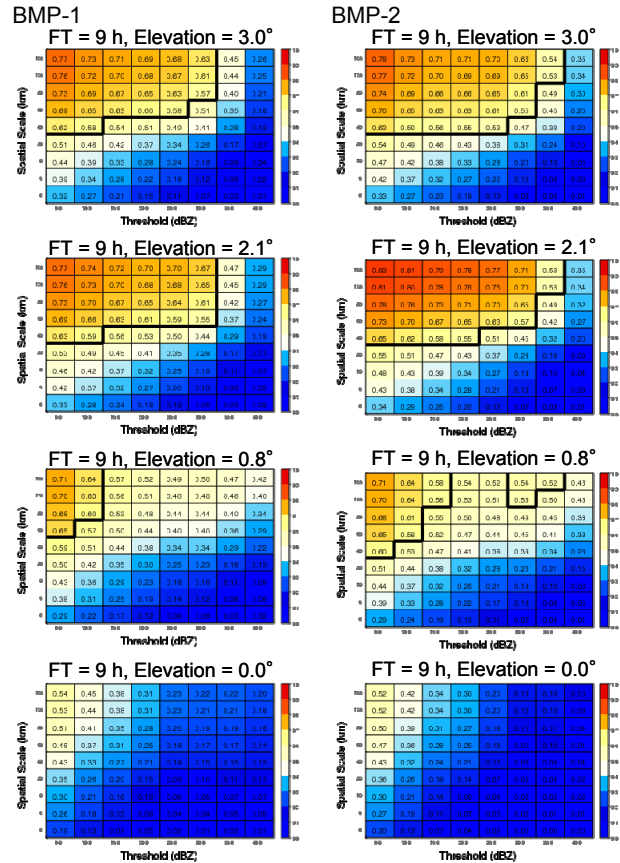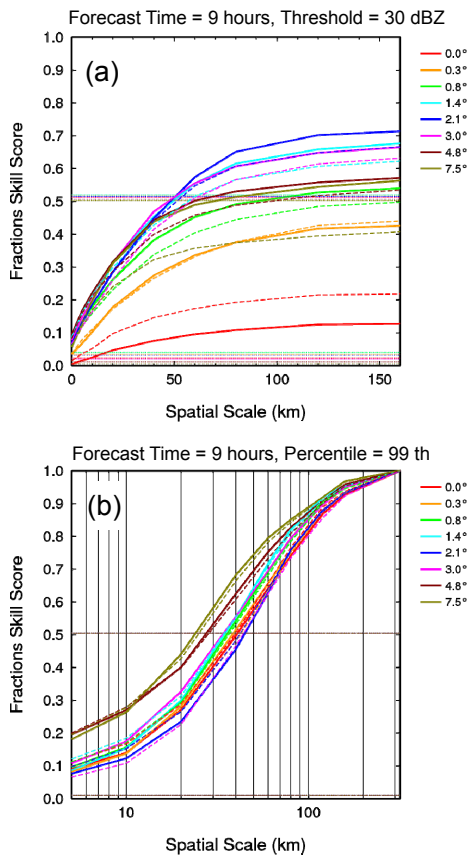
Figure 1: FSS for FT = 9 hours: (a) threshold 30 dBZ, and (b) 99th percentile. The elevation levels are 0.0°, 0.3°, 0.8°, 1.4°, 2.1°, 3.0°, 4.8° and 7.5°. The solid lines are BMP-2, and the dashed lines are BMP-1.

Figure 2: FSS diagrams: experiments for (left) BMP-1, and (right) BMP-2. The bold black lines show the target skill in each diagram. The thresholds are 5.0, 10.0, 15.0, 20.0, 25.0, 30.0, 35.0 and 40.0 dBZ, and the spatial scales are 5, 15, 25, 45, 85, 125, 165, 245 and 325 km.

References

Roberts, N. M. and H. W. Lean, 2008: Scale-selective verification of rainfall accumulations from high-resolution forecasts of convective events. *Mon. Wea. Rev.*, 136, 7897.

Saito, K., T. Fujita, Y. Yamada, J. Ishida, Y. Kumagai, K. Aranami, S. Ohmori, R. Nagasawa, S. Kumagai, C. Muroi, T. Kato, H. Eito and Y. Yamazaki, 2006: The Operational JMA Nonhydrostatic Mesoscale Model., *Mon. Wea. Rev.*, 134, 1266-1298.

Honda, Y., M. Nishijima, K. Koizumi, Y. Ohta, K. Tamiya, T. Kawabata and T. Tsuyuki, 2005: A pre-operational variational data assimilation system for a non-hydrostatic model at the Japan Meteorological Agency: Formulation and preliminary results. *Quart. J. Roy. Meteor. Soc.*, 131, 3465-3475.

Caumont, O. and Coauthors, 2006: A radar simulator for high-resolution nonhydrostatic models. *J. Atmos. Oceanic Technol.*, 23, 1049-1067.

Development of a New Nonhydrostatic Model ASUCA at JMA

Junichi Ishida[1], Chiashi Muroi[1], Kohei Kawano[1], Yuji Kitamura[2]

[1]*Numerical Prediction Division, Japan Meteorological Agency,* [2]*Meteorological Research Institute*

j_ishida@naps.kishou.go.jp, cmuroi@naps.kishou.go.jp, kkawano@naps.kishou.go.jp, kitamura@mri-jma.go.jp

1 Introduction

The Japan Meteorological Agency (JMA) operates a nonhydrostatic regional model (NHM) with a horizontal resolution of 5 km. In recent years, new nonhydrostatic equations which conserve mass and some highly efficient numerical methods in fluid dynamics have been widely used in numerical weather prediction models. This has motivated us to develop a new dynamical core.

This new core is intended to achieve higher accuracy and improved computational stability. The core and program code are designed to be efficient for massively parallel machines. The new dynamical core is named ASUCA.

2 Outline of ASUCA

ASUCA employs generalized coordinates $(\hat{x}^1, \hat{x}^2, \hat{x}^3)$. Using the Einstein summation convention, its flux-form nonhydrostatic equations are written as follows:

$$\frac{\partial}{\partial t}\left(\frac{\rho u^i}{J}\right) + \frac{\partial}{\partial \hat{x}^j}\left(\frac{\rho u^i \hat{u}^j}{J}\right) + \frac{\partial}{\partial \hat{x}^n}\left(\frac{1}{J}\frac{\partial \hat{x}^n}{\partial x^i}p\right)$$
$$- \frac{\rho g^i}{J} = \frac{F^i}{J},$$

$$\frac{\partial}{\partial t}\left(\frac{\rho}{J}\right) + \frac{\partial}{\partial \hat{x}^i}\left(\frac{\rho \hat{u}^i}{J}\right) = \frac{F_\rho}{J},$$

$$\frac{\partial}{\partial t}\left(\frac{\rho \theta_m}{J}\right) + \frac{\partial}{\partial \hat{x}^i}\left(\frac{\rho \theta_m \hat{u}^i}{J}\right) = \frac{F_{\rho \theta_m}}{J},$$

$$\frac{\partial}{\partial t}\left(\frac{\rho q_x}{J}\right) + \frac{\partial}{\partial \hat{x}^i}\left(\frac{\rho q_x \hat{u}^i_x}{J}\right) = \frac{F_{\rho q_x}}{J},$$

$$p = R_d \pi \left(\rho \theta_m\right),$$

where u, v, w and $\hat{u}, \hat{v}, \hat{w}$ represent the velocity components in Cartesian coordinates and generalized coordinates, respectively, J is the Jacobian of coordinate transformation, π is the Exner function, ρ is the total mass density, and q_x is the ratio of the density of water substance x to the total mass density (for example, q_v for water vapor, q_c for cloud water and so on). In order to use the same state equation in the dry and moist system, $\theta_m = \theta(\rho_d/\rho + \epsilon \rho_v/\rho)$ is introduced, where ϵ is the ratio of R_v to R_d. The velocity $\hat{u}^i_x$ in the equation for water substances may be different from the velocity of the atmosphere if terminal fall velocity exists. The right hand side of each equation F contains not only the Coriolis force, diffusion and diabatic effects but also terms arising from the density change due to precipitation.

The equations are discretized using the finite volume method (FVM). The flux limiter function proposed by Koren (1993) is employed for monotonicity to avoid numerical oscillations. A third-order Runge-Kutta scheme is adopted for the time integration of the system. The terms responsible for sound waves and gravity waves are treated using a split-explicit time integration scheme. For the short time step, a second-order Runge-Kutta scheme is employed. Another time-splitting method is also used to treat the vertical advection of water substances with a high terminal velocity (such as rain or graupel). Since it is only limited by the vertical CFL condition, a short time step interval is determined in each column.

The Deardorff model (Deardorff, 1980) is implemented to represent the effects of turbulent motions that cannot be resolved in the numerical model. In this model, eddy flux is parameterized in terms of eddy viscosity and eddy thermal diffusivity, and these coefficients are determined as a function of the mixing length l and the turbulent kinetic energy (TKE) E, which is regarded as a prognostic variable. The TKE equation is described as

$$\frac{\partial}{\partial t}\left(\frac{\rho E}{J}\right) + \frac{\partial}{\partial \hat{x}^j}\left(\frac{\rho E \hat{u}^j}{J}\right) = P + D - \epsilon.$$

Here, P, D and ϵ denote the TKE production, diffusion and dissipation terms, and are parameterized as

$$P = \frac{\rho}{J}\left[K_m\left(\frac{\partial \hat{x}^k}{\partial x^j}\frac{\partial u^i}{\partial \hat{x}^k} + \frac{\partial \hat{x}^k}{\partial x^i}\frac{\partial u^j}{\partial \hat{x}^k}\right) - \frac{2}{3}\delta^j_i E\right]\frac{\partial \hat{x}^l}{\partial x^j}\frac{\partial u^i}{\partial \hat{x}^l}$$
$$- \frac{g}{\theta_v}\frac{\rho}{J}K_h \frac{\partial \hat{x}^k}{\partial x^3}\frac{\partial \theta_v}{\partial \hat{x}^k},$$

$$D = \frac{\partial}{\partial \hat{x}^l}\left(\frac{2K_m}{J}\frac{\partial \hat{x}^l}{\partial x^i}\frac{\partial \hat{x}^k}{\partial x^i}\frac{\partial \rho E}{\partial \hat{x}^k}\right),$$

$$\epsilon = \frac{C_\epsilon \rho E^{3/2}}{lJ}.$$

K_m and K_h represent the eddy viscosity and eddy thermal diffusivity coefficients, respectively. It should be noted that the prognostic equation for $\rho E/J$ instead of E is solved in ASUCA so that the advection term in the TKE equation can be treated as the flux-form in the generalized coordinates. The mixing length l is diagnosed using the formula proposed by Sun and Cheng (1986). The vertical diffusion and the TKE dissipation terms are evaluated with the implicit scheme in order to avoid computational instability.

3   Experiment results

A numerical experiment for nonhydrostatic scale inertia gravity waves, originally proposed by Skamarock and Klemp (1994), was carried out. The configurations used were identical to those in their paper with the exception of the time step of ASUCA, which was 60 s. The left and right parts of Fig. 1 show the numerical solutions obtained using ASUCA and the analytical solution, respectively. The numerical result is quite similar to the analytical solution.

The results of another numerical experiments for non-linear density current in which the result obtained by Straka et al. (1993) is usually used as a benchmark are shown in Fig. 2. The time steps are 1 s for $\Delta x = 50$ m and 2 s for $\Delta x = 100$ m. Both results are comparable to those of the benchmark.

4   Conclusions

We have developed a new dynamical core and turbulent model. A number of idealized experiments were conducted, and the results indicate a high level of performance. The computational efficiency of ASUCA is now being tested both on a GPU (Shimokawabe et al., 2010) and on JMA's super computer system.

The next target of our development is to test the dynamical core extended to the moist system and to develop physics processes for operational purposes. Though the NHM has a lot of physics schemes, which have been well tested operationally,

we plan to evaluate them carefully and employ only useful schemes for ASUCA.

References

Deardorff, J. W., 1980: Stratocumulus-capped mixed layers derived from a three-dimensional model. *Boundary-Layer Meteorol.*, **18**, 495–527.

Koren, B., 1993: A Robust Upwind Discretization Method for Advection, Diffusion and Source Terms. *CWI Report NM-R9308.*

Shimokawabe, T., T. Aoki, J. Ishida, and C. Muroi, 2010: GPU Acceleration of Meso-scale Atmosphere model ASUCA. *CAS/JSC WGNE Research Activities in Atmospheric and Oceanic Modelling.*

Skamarock, W. C. and J. B. Klemp, 1994: Efficiency and accuracy of the Klemp-Wilhelmson time-splitting technique. *Mon. Wea. Rev.*, **122**, 2623–2630.

Straka, J. M., R. B. Wilhelmson, L. J. Wicker, J. R. Anderson, and K. K. Droegemeier, 1993: Numerical solutions of a non-linear density current: a benchmark solution and comparisons. *Intl. J. Numerical Methods in Fluids*, **17**, 1–22.

Sun, W. Y. and C. Z. Cheng, 1986: Diffusion model for a convective layer. Part I: Numerical simulation of convective boundary layer. *J. Climate Appl. Meteor.*, **25**, 1445–1453.
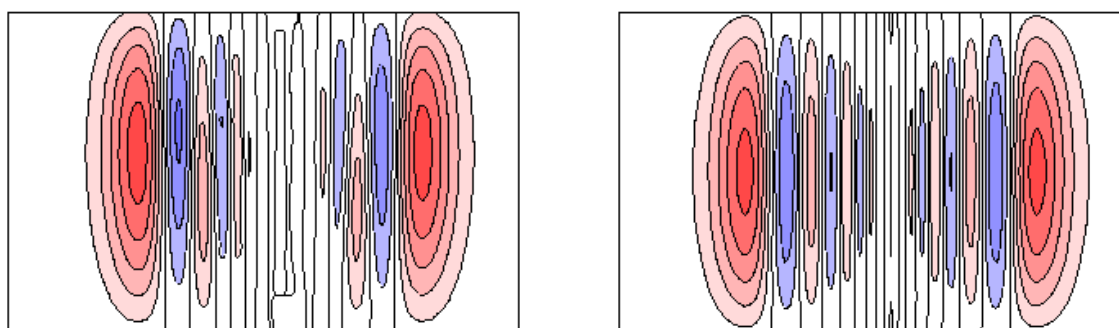
Figure 1: Inertia gravity test by Skamarock and Klemp (1994): Perturbation of θ at $t = 3000$ s of the numerical solution by ASUCA (left) and the analytical solution(right).

Figure 2: Non-linear density current test by Straka et al. (1993): Contours of θ at $t = 15$ min. The region is the same as that in Fig. 1 for Straka et al. (1993). The figures show the results obtained using ASUCA with $\Delta x = 50$ m (left) and $\Delta x = 100$ m (right).

Experimental operation of a high-resolution local forecast model at JMA (3)

Takahisa Ishimizu and Masashi Ujiie

Numerical Prediction Division, Japan Meteorological Agency,
1-3-4 Otemachi, Chiyoda-ku, Tokyo 100-8122, Japan
E-mail: ishimizu@naps.kishou.go.jp

1. Introduction

The Numerical Prediction Division of the Japan Meteorological Agency is developing a model called the LFM (Local Forecast Model).The purposes of the LFM are to contribute to aviation forecasting and more detailed information for disaster prevention.

The LFM is based on JMA-NHM (Saito et al., 2006) with a horizontal grid spacing of 2km. The LFM has been applied to improvement of the operational 5km-mesh meso-scale model, the MSM (Hara et al., 2007). As a part of the development, the NPD/JMA has experimentally operated the LFM since July 2007 (Nakayama et al., 2007), and verification around Tokyo international airport has been examined.

2. Enhancements in 2009

(1) Treatment of cumulus scheme

To suppress excessive rainfalls such as a grid point storm, a modified version of the Kain-Fritsch scheme was temporarily used for the LFM (Takenouchi et al., 2008). The LFM is not currently being run with the Kain-Fritsch scheme to seek more adequate schemes.

(2) Enlargement of computational domain

To reduce the effects of the lateral boundary condition, we enlarged the domain to the west to cover the western part of Japan in August 2009 (shown in Figure 1). Since then, unrealistic convergence lines (Ujiie et al., 2009) have not appeared so far. But it is necessary to monitor the situation to watch for their possible appearance.

(3) A new high performance computer

Three nodes of the SX-9 were installed in March 2009. Since the system transition, we have run the experimental LFM on a new high performance computer.
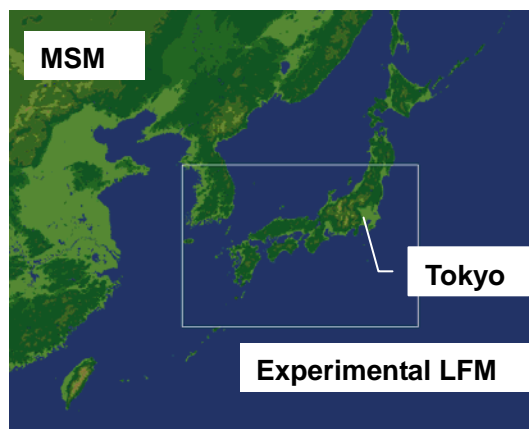
Figure 1: Experimental LFM and MSM domain

3. Specifications of experimental LFM

Table 1: Specifications of the experimental LFM

	LFM (August 2009)
Horizontal mesh	800 x 550
Resolution	2km
Vertical layers	60 (top level 20km)
Time interval	8 seconds
Forecast period	12 hours
Run frequency	4 times a day
Initial conditions	JNoVA-3DVar*
Lateral boundary	MSM
Boundary layer	Improved Mellor-Yamada Level3
Moist physics	3 ice bulk microphysics (snow, ice, graupel)
Cumulus Parameterization	Not used

*JNoVA is the JMA Nonhydrostatic Model-based Variational Data Assimilation System. The LFM initial condition is prepared using a rapid update cycle with the 3D-Var version of JNoVA, which assimilates surface observations (wind and temperature) and vertical wind fields (wind profilers, doppler radars and ACARS).

4. Case Study

Figure 2 shows a case with synoptic scale disturbances accompanying a cold front that passed over Japan. The experimental LFM represented rainfall better than the MSM on southern slopes of terrain. This is because of the differences in horizontal resolutions and the treatment of cumulus schemes between the LFM and the MSM.
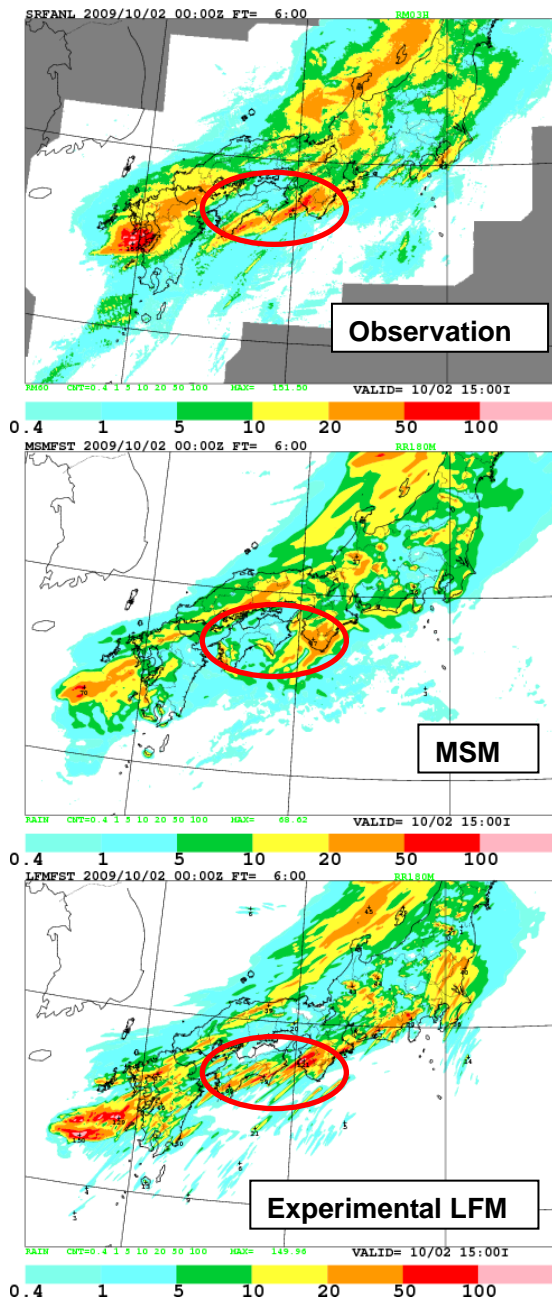
Figure2: Precipitation [mm/3hours] is shown with coloured shading. Top: precipitation analyzed by surface observation and radar, Middle: MSM (JMA operational 5km-mesh meso-scale model), Bottom: experimental LFM (INIT2009/10/02 00 UTC, FT=6).

5. Future plans and issues

The JMA is planning to operate a 2km-mesh meso-scale model over all Japan from 2013. However, case studies have revealed a few issues, delay of rainfall beginnings, overly intense convection to make local circulation worse (Ujiie et al., 2009) affecting vertical profiles of the atmosphere. To represent more accurate precipitation and vertical profiles, we should improve the related physical processes and verify the initiation timing of convection.

References

Nakayama, H., Y. Ishikawa, T. Fujita and K. Takenouchi, 2007 : Experimental operation of a high-resolution local forecast model at JMA. *CAS/JSC WGNE Res. Activ. Atmos. Oceanic Modell.*, **37**, 0519-0520.

Kensuke Takenouchi, Haruka Kurahashi, Tadashi Fujita and Kohei Aranami, 2008 :   Experimental operation of a high-resolution local forecast model at JMA(2). *CAS/JSC WGNE R*es*. Activ. Atmos. Oceanic Modell.*, **38**, 0523-0524.

Saito, K., T. Fujita, Y. Yamada, J. Ishida, Y. Kumagai, K. Aranami, S. Ohmori, R. Nagasawa, S.Kumagai, C. Muroi, T. Kato, H. Eito and Y. Yamazaki 2006: The operational JMA Non-hydrostatic Mesoscale Model. *Mon. Wea. Rev.*, **134**, 1266-1298.

Hara, T., K. Aranami, R. Nagasawa, M. Narita, T. Segawa, D. Miura, Y. Honda, H. Nakayama, and K. Takenouchi, 2007: Upgrade of the operational JMA non-hydrostatic mesoscale model. *CAS/JSC WGNE Res. Activ. Atmos. Oceanic Modell.*, **37**, 0511-0512.

Ujiie, M., H. Kurahashi and K. Aranami, 2009: Performance of a high resolution local forecast model of the JMA on torrential rains forecast: *8th International SRNWP-Workshop on Non-Hydrostatic Modelling*.

Precipitation Efficiency in Numerically Simulated Heavy Rainfall Associated with Typhoons Man-Yi (2007) and Fitow (2007)

Akihiko MURATA

Meteorological Research Institute / Japan Meteorological Agency, Tsukuba, Ibaraki 305-0052, Japan

1. Introduction

Heavy rain accompanying tropical cyclones risks the life of many people and causes widespread material damage. It is therefore very important to evince the mechanisms of heavy precipitation associated with tropical cyclones. Typical precipitation accompanying tropical cyclones is associated with the eyewall or spiral rainbands.

There exists another type of rainfall associated with tropical cyclones: the area of heavy precipitation is farther from the storm center. For instance, an extremely heavy precipitation event associated with typhoon Meari in 2004 in a mountainous region in Japan characterized that the area of precipitation is 500 km farther from the storm center (Murata 2009; refereed to as M2009). M2009 demonstrated that a mechanism of the heavy precipitation is associated with higher efficiency of precipitation, which is attributed to higher rate of the conversion of could water to rain water via accretion of cloud water by rain, under the condition of intense water vapor flux convergence. It is interesting to compare these findings with those in other heavy precipitation events that occurred far from the tropical cyclone center. The comparison enables us test whether the mechanism holds in those different cases.

2. Numerical model and experimental design

The numerical model used is the Japan Meteorological Agency Nonhydrostatic Model (JMANHM; Saito et al. 2006). The horizontal grid has 701x701 grid points and the grid spacing is 1 km. The vertical coordinate is terrain-following and contains 50 levels, with variable grid intervals of 40 m to 904 m. The lowest level is located at 20 m from ground surface, whereas the highest level is at 22 km. The time-step intervals are 5 s. The initial and boundary data are provided by the JMA mesoscale analysis data.

3. Cases

3-1 Typhoon Man-Yi (2007)

Heavy rainfall in the southeastern part of Kyushu, a southwestern part of Japan, started more than 24 h before the typhoon landfall. Observed 1-h accumulated rainfall amounts at Hyuga, located in a southeastern part of Kyushu (32.4N, 131.6E), demonstrated that the present heavy precipitation event is extreme on a short time scale (not shown). For example, data showed 84 mm per 1 hour between 0950 and 1050 JST 13 July.

3-2 Typhoon Fitow (2007)

Heavy rainfall in the northeastern part of Honshu, the mainland of Japan, started more than 24 h before the typhoon landfall. Observed 1-h accumulated rainfall amounts at Hippo, located in a northeastern part of Honshu (37.8N, 140.7E), demonstrated that the present heavy precipitation event is extreme on a short time scale (not shown). For example, data showed 83 mm per 1 hour between 2040 and 2140 JST 5 September.

4. Results

Because extremely heavy precipitation was observed around Hyuga (Hippo) associated with typhoon Man-Yi (Fitow), a 60-km square area centered on Hyuga (Hippo) is set for calculating precipitation efficiency. The time series of variables, regarding precipitation efficiency, horizontally averaged over the area are shown in Fig. 1. The variables include water vapor flux convergence, the

sum of condensation and deposition, and precipitation, where the former two are vertically integrated variables and the latter is the variable observed at the surface.

Three kinds of precipitation efficiency used are defined as follows: 1) Condensation efficiency (CE): The sum of vertically accumulated condensation and deposition divided by vertically accumulated water vapor flux convergence, 2) Rainfall efficiency (RE): The amount of rainfall reaching the ground divided by the sum of vertically accumulated condensation and deposition, and 3) Multiplied efficiency (ME): The amount of rainfall reaching the ground divided by vertically accumulated water vapor flux convergence. ME therefore is the product of CE and RE. Two periods are considered for calculating the precipitation efficiencies as follows: 0400-0600 JST and 0600-0800 JST for the Man-Yi case and 1600-2100 JST and 2100-0200 JST for the Fitow case. The latter (former) period in each case corresponds to that when relatively heavy (light) precipitation occurred.

The calculated precipitation efficiencies show that ME in the latter period has higher value than that in the former period in both cases (Fig. 2). The period of the higher ME corresponds to that of heavier rains. The difference in ME between the two periods is attributed to those in both CE and RE. The results suggest that condensation and deposition occur efficiently in addition to efficient production of rainwater by cloud microphysical processes, whereas only the latter effect was dominant in M2009. The structure of precipitation systems may be responsible for the relative importance of CE or RE. More detailed work is necessary to resolve this issue.

References

Murata, A., 2009: A mechanism for heavy precipitation over the Kii Peninsula accompanying typhoon Meari (2004). J. Meteor. Soc. Japan, 87, 101-117.

Saito, K., T. Fujita, Y. Yamada, J. Ishida, Y. Kumagai, K. Aranami, S. Ohmori, R. Nagasawa, S. Kumagai, C. Muroi, T. Kato, H. Eito and Y. Yamazaki, 2006: The operational JMA Nonhydrostatic Mesoscale Model. Mon. Wea. Rev., 134, 1266-1298.
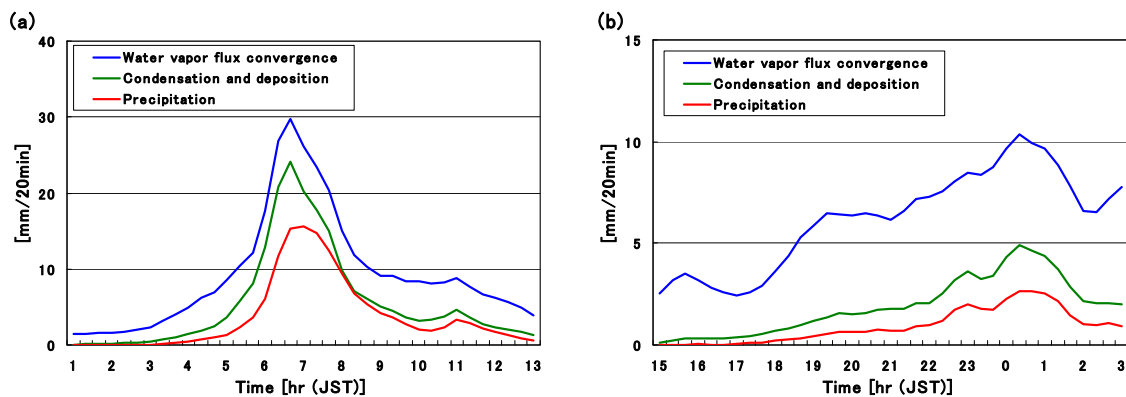
Fig.1 Time series of precipitation, the sum of condensation and deposition, and water vapor flux convergence for the cases of (a) typhoon Man-Yi (from 0100 to 1300 JST 13 July 2007) and (b) typhoon Fitow (from 1500 JST 5 September to 0300 JST 6 September 2007).
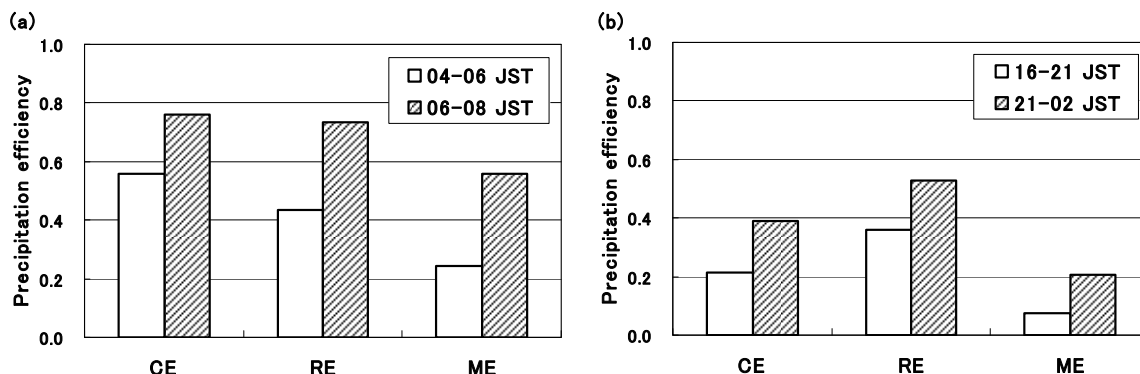
Fig.2 Condensation efficiency (CE), rainfall efficiency (RE), and multiplied efficiency (ME) for the cases of (a) typhoon Man-Yi and (b) typhoon Fitow.

Development of a Mesoscale Ensemble Prediction System Using a Singular Vector Method

Kosuke Ono*, Yuki Honda*, Masaru Kunii**

*Numerical Prediction Division, Japan Meteorological Agency, Tokyo, Japan
**Typhoon Research Department, Meteorological Research Institute, Tsukuba, Japan
E-mail: kou.ono@met.kishou.go.jp

Since April 2007, we have been developing a mesoscale ensemble prediction system using a singular vector (SV) method to provide probabilistic information and multi-scenarios for operational mesoscale forecasting (MSM). To calculate perturbations, two singular vector methods are under trial. One is the mesoscale singular vector (MSV) method using the tangent linear model and its adjoint model based on the JMA nonhydrostatic model (JMA-NHM). The other is the global singular vector (GSV) method using the tangent linear model and its adjoint model based on the JMA global spectral model.

We are conducting four ensemble forecast experiments with different initial perturbations targeting the heavy rain associated with the Baiu front. First, we calculate the initial perturbations using the high-resolution MSV (with a horizontal grid spacing of 40 km and an optimization time of 15 hours: MSV40). The initial perturbations of MSV40 are more localized due to its higher resolution. These localized perturbations are effective in providing a suitable scale against the forecast of the mesoscale phenomenon, but are not effective for calculating scores estimated over a large verification area. For this reason, a combination of localized and non-localized perturbations is required. Accordingly, we calculate the low-resolution MSV (with a horizontal grid spacing of 80 km and an optimization time of 15 hours: MSV80). In order to combine the fine structure of MSV40 with the broad structure of MSV80, we blend MSV40 using a six-hour optimization time with MSV80 (BSV). Finally, for comparison, we use GSV with an optimization time of 24 hours. In all singular vector calculations, moist physics are used in the tangent linear and adjoint models, and the target area is the region around Japan (125 – 145°E, 25 – 45°N). Moist total energy is also used as the initial and final norm. Each ensemble forecast consists of 11 members (including a control forecast) using JMA-NHM with a horizontal resolution of 20 km.

Figure 1 shows the distribution of rainfall for observation and the six-hour forecast of the MSM along with the control forecast on 28 June 2008. The MSM and the control forecast, with horizontal resolutions of 5 km and 20 km, respectively, cannot predict the heavy rain around western Japan and the islands to the southwest. Figure 2 shows the ensemble spread of rainfall. A large spread for MSV40 and BSV is seen where light rainfall is predicted by the control forecast, while observed rainfall is heavy in other areas such as the islands to the southwest. It is suggested that the ensemble forecasts indicate the uncertainty of the control forecast and the potential area of observed heavy rain. Figure 3 shows the initial perturbations of each experiment. MSV40 has a fine structure, but is localized. MSV80 has a coarser and broader distribution than MSV40, and BSV has a fine and broad structure. GSV has the broadest structure. In this case, it seems that the size of the heavy-rain area is so small that only the experiments adopting initial perturbations with a fine structure can show heavy-rain potential.

Figure 4 shows the ROC area skill score for each experiment. The verification period is from 24 to 30 June 2008, and each initial is 18 UTC (a total of seven cases). In the first half of the forecast period, MSV80 is better than MSV40. MSV40 has a fine structure that is suitable for mesoscale phenomena, but as previously mentioned, in the case of a large verification area, it is inferior to MSV80. BSV can overcome this problem, and has the best score in the first half of the forecast period. In the latter half of the forecast, GSV is the best. This is because it has the broadest horizontal distribution and its perturbations are effective within the verification area in the latter half of the forecast period.

Next, to consider the uncertainty of the lateral boundary condition, we are developing lateral boundary perturbation using GSV as follows: Firstly, we calculate five GSVs, and then calculate a control run for the low-resolution JMA-NHM and five perturbed runs with a horizontal resolution of 40 km. Finally, we calculate the differences between the control run and the perturbed runs. Figure 5 shows an example of an ensemble forecast with lateral boundary perturbation. It can be seen that in the forecasted area of heavy rain near the boundary, the experiment with lateral boundary perturbation shows a large spread of three-hour accumulated precipitation (18 UTC July 2009, FT = 24). This is because lateral boundary perturbations affect the forecast

region through the lateral boundary. Combining the initial perturbations of MSV with the lateral boundary perturbations, we can expect an improvement of the score in the latter half of the forecast period.
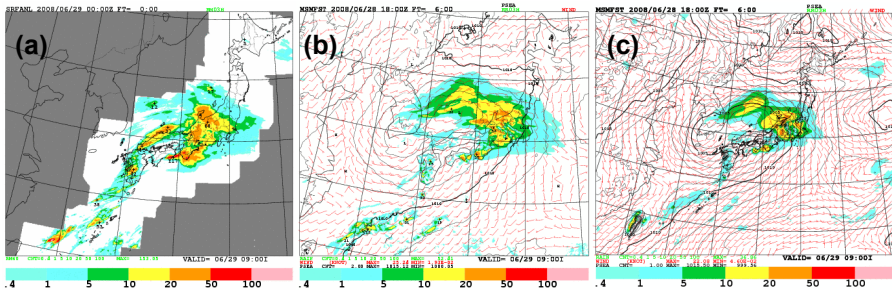
Fig 1. Distribution of three-hour accumulated precipitation [mm/3 h] at 00 UTC on 29 June 2009: (a) observation; (b) operational MSM (FT = 6); (c) control forecast (FT = 6)
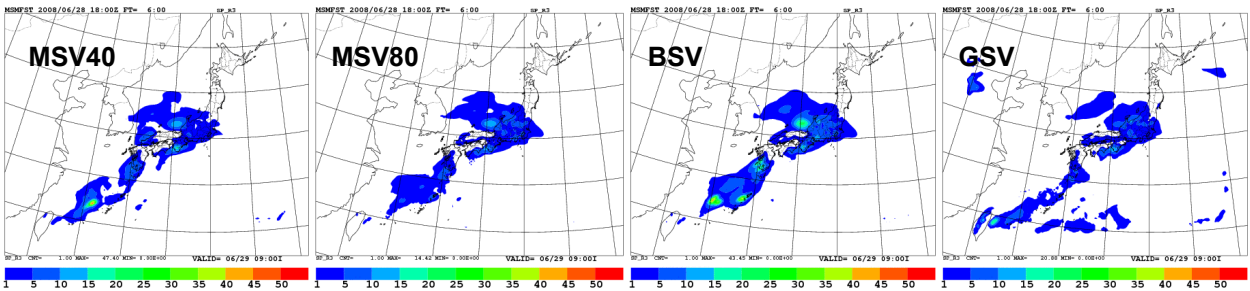
Fig 2. Ensemble spread of three-hour accumulated precipitation [mm/3 h]. FT = 6
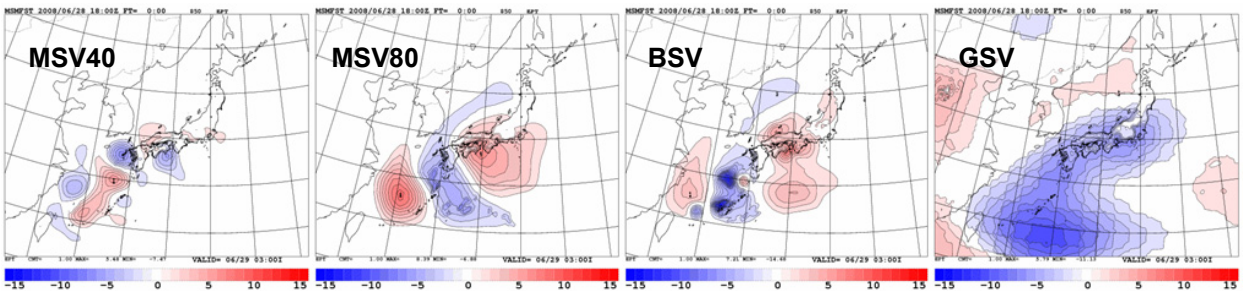
Fig 3. Initial perturbation of equivalent potential temperature at 850 hPa [K]
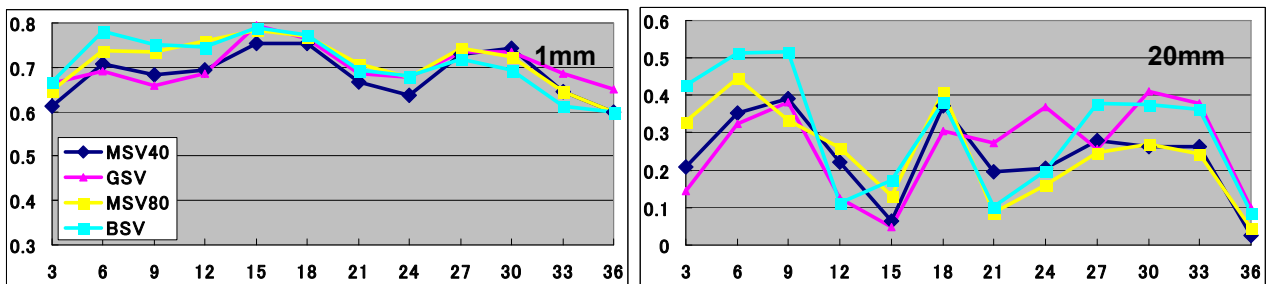
Fig 4. ROC area skill score for three-hour accumulated precipitation. The horizontal axis represents the forecast time.
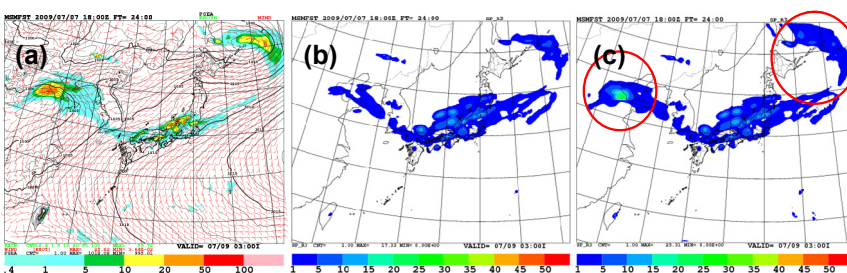
Fig 5. (a) Forecasted rainfall of the control run. (b) Ensemble spread of rainfall without lateral boundary perturbation [mm/3 h]. (c) As per (b), but with lateral boundary perturbation. The initial is 18 UTC on 7 July 2009. FT = 24.

Generation mechanisms of convections by gravity waves

HIROMU SEKO, SYUGO HAYASHI and KAZUO SAITO

Meteorological Research Institute

1. Introduction

Because convective storms sometime cause mudslides or floods, it is important to understand the generation and development mechanisms of the convections. In this study, the generation mechanisms of the convections by gravity waves (GWs) were investigated using the outputs of Non-hydrostatic model (NHM).

2. Ideal experiment of 2-dimensional model

To understand the generation process of convections, ideal experiments using 2-dimensional model was performed (Yamasaki and Seko, 1992). Typical profiles of temperature and humidity in the tropical atmosphere were used as the basic fields. Two sets of four babbles were placed in the domain of numerical model.

Figure 1 shows the temporal variations of vertical wind at z=1.2km and temperature at z=150 m. GWs were generated at the convections and propagated from the convections. Convection **F** was generated at the overlapped area of GWs from the convections **A** and **C**. Convection **F** was developed when GWs from the convections **B** and **E** arrived. Convection **J** was also generated when GW arrived from the convection **G**, and was developed when GW arrived from the convection **H**. When GW approached, temperature was decreased and relative humidity was increased (not shown). Updraft of GW and these changes caused by GWs are the favorable conditions for the generation and development of convections. There was no cold pool where convections **F** and **J** were generated. This distribution indicates that GW generates and develops the convections.

3. Generation mechanisms of convections by gravity waves

Numerical simulations using NHM were performed from the initial conditions produced from JRA25 data. Initial time was 12UTC 28 2008. Downscale experiments were further performed with the grid intervals of 5 km and 1 km.

Figure 2a shows the rainfall distribution reproduced by 5km-NHM. A convective band extending southeastward was generated at the eastern side of Sumatra Island. Figures 2b and 2c are the distributions of rainfall and temperature at P=1000hPa, reproduced by 1km-NHM. Convection **A** was generated on the eastern side of the convective band in the convergence zone of

northwesterly and westerly flows (Fig. 2a). When convection **A** was generated, the cold pool did not exist near the convection **A**. The convections were generated at the eastern side of the band successively. Convections **B** at the southern side of the convective band were generated at the gradient zone of temperature. This gradient was the boundary of the cold pool, which was expanding eastward. This distribution suggests that the cold pool also contributed the generation of the convection. Figure 3 is the time sequence of vertical wind, temperature and dew-point deficit (T-Td) at P=950hPa along the broken line in Fig. 1b, which crossed the convection **A**. Convection **A** was generated at the weak updraft region along the eastern side of the band (dotted line in Fig. 3c), when GW was propagated from the east (broken line in Fig. 3a). When GW was propagated, temperature was decreased and dew-point deficit became smaller (Figs. 3b and 3d). The updraft of GW makes the atmosphere cooler and moister, which are favorable conditions for the generation and development of convections.

Figure 4 is the same as Fig. 3 except for the broken line in Fig. 2c, which crossed the convections **B**. Convections **B** were generated along the edge of the cold pool (dotted line in Fig. 4c). Low-level updraft was produced by the
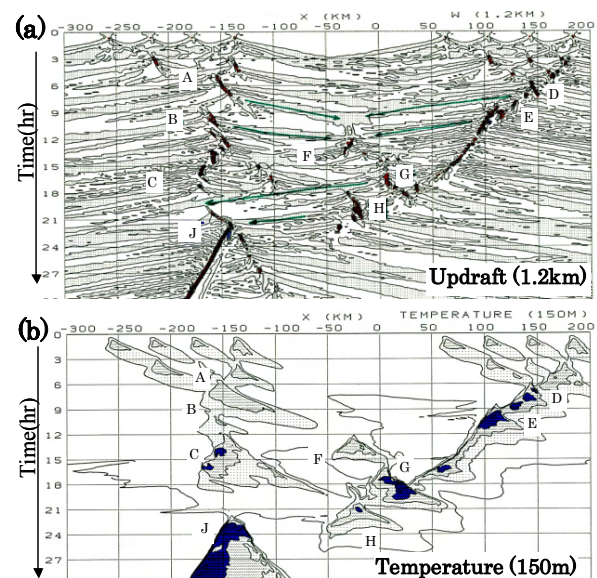
Fig. 1 Time sequence of (a) updraft at z=1.2km and (b) temperature at 150m (After Yamasaki and Seko,1992).

outflow of the cold pool. When the gravity wave from the western side overlapped the edge of cold pool, the convection was generated (broken line in Fig. 4a). These variations of temperature and dew-point deficit were also common with the convection A (Figs. 4b and 4d).

4. Summary

Updraft of GW makes the atmosphere cool and moistens. Updraft and these changes are favorable conditions for the generation of convections. When the weak convergence or weak cold pools exists, GW determines the generation point and timing of convection.

References

Yamasaki, M., and H. Seko, Effect of the gravity wave on the convections, 1992, Proceedings of Spring meeting of Meteorological Society of Japan, A108 (in Japanese).
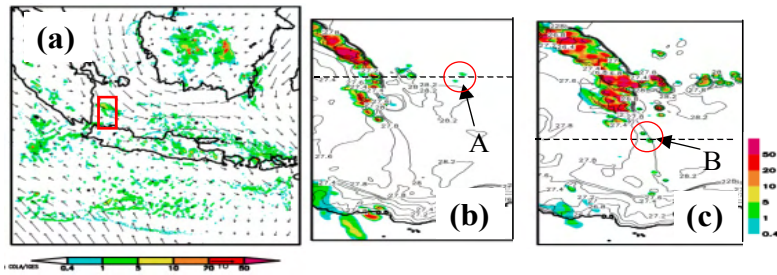
Fig. 2 (a) Rainfall region reproduced by 5km-NHM. Initial time is 18UTC 28 Jan. 2008. Rainfall region and temperature at 1000hPa at (b) 22:30UTC 29 and (c) 23:20UTC reproduced by 1km-NHM. Domains of (b) and (c) are indicated by rectangle in (a). Initial time of 1km-NHM is 15UTC 29.
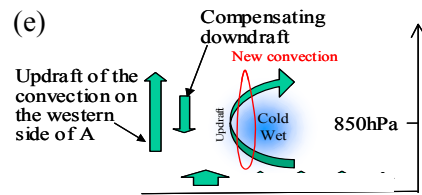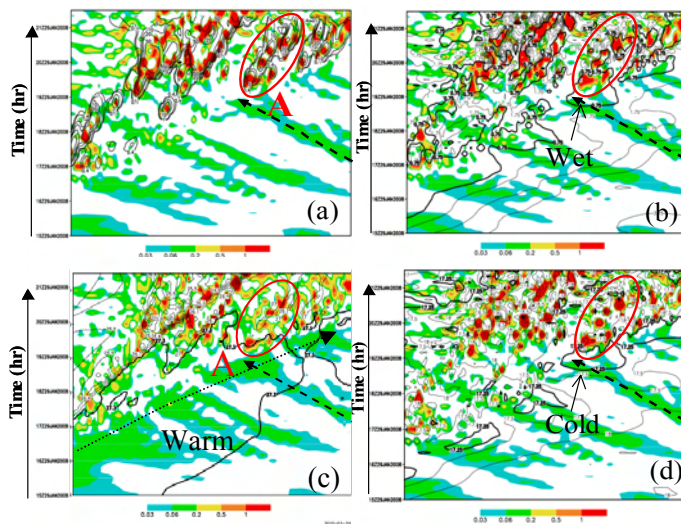
Fig. 3 Time variation of updraft (colored region) at (a, b and d) P=850hPa and (c) P=925hPa along the broken line in Fig. 2b and, (a) rainfall (b) dew-point deficit at P=850hPa, (c) temperature at P=1000hPa and (d) temperature at P=850hPa. (e) Schematic illustration of convections A.
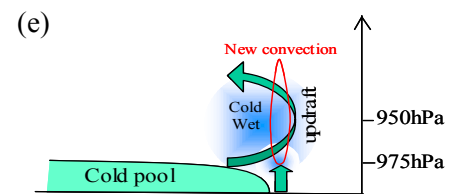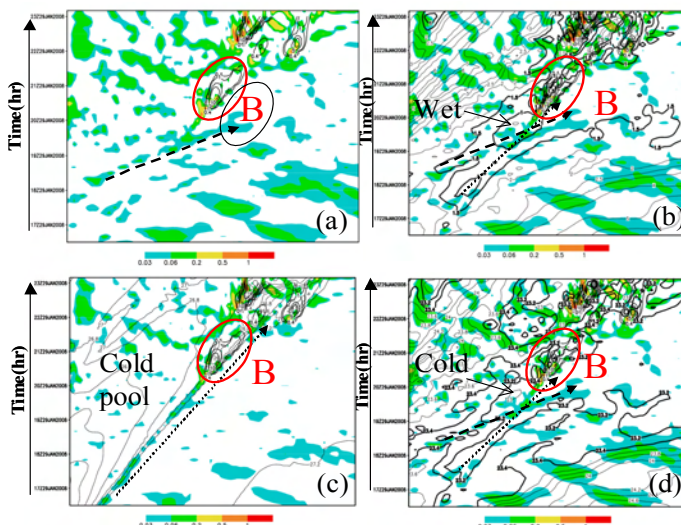
Fig. 4 Time variation of updraft (colored region) at (a, b and d) P=950hPa and (c) 975hPa along the broken line in Fig. 2c, (a) rainfall (b) dew-point deficit at P=950hPa, (c) temperature at P=1000hPa and (d) temperature at P=950hPa. (e) Schematic illustration of convections B.